High-contrast Hα imaging with Subaru/SCExAO + VAMPIRES

**Taichi Uyama[a,b,c,*] Barnaby Norris,[d,e] Nemanja Jovanovic[f]
Julien Lozi[g] Peter Tuthill,[d] Olivier Guyon[g,h,i] Tomoyuki Kudo,[f]
Jun Hashimoto[i] Motohide Tamura,[c,i,j] and Frantz Martinache[k]**

[a]California Institute of Technology, Infrared Processing and Analysis Center, Pasadena, California, United States
[b]NASA Exoplanet Science Institute, Pasadena, California, United States
[c]National Astronomical Observatory of Japan, Tokyo, Japan
[d]University of Sydney, Sydney Institute for Astronomy, School of Physics, Sydney, New South Wales, Australia
[e]University of Sydney, Australian Astronomical Observatory-University of Sydney, School of Physics, Sydney, New South Wales, Australia
[f]California Institute of Technology, Department of Astronomy, Pasadena, California, United States
[g]National Astronomical Observatory of Japan, Subaru Telescope, Tokyo, Japan
[h]University of Arizona, Steward Observatory, Tucson, Arizona, United States
[i]Astrobiology Center of NINS, Tokyo, Japan
[j]The University of Tokyo, Department of Astronomy, Tokyo, Japan
[k]University Côte d'Azur, Observatoire de la Côte d'Azur, French National Center for Scientific Research, Laboratoire Lagrange, Biot, France

Abstract. We present the current status of Hα high-contrast imaging observations with Subaru/Subaru Coronagraphic Extreme Adaptive Optics + VAMPIRES. Our adaptive optics correction at optical wavelengths in combination with (double) spectral differential imaging (SDI) and angular differential imaging (ADI) was capable of resolving a ring feature around omi Cet and detect the Hα counterpart of jet around RY Tau. We tested the post-processing by changing the order of ADI and SDI and both of the contrast limits achieved $\sim 10^{-3}$ to 5×10^{-4} at $0.3''$, which is comparable to other Hα high-contrast imaging instruments in the Southern Hemisphere such as very large telescope (VLT)/spectro-polarimetric high-contrast exoplanet research, VLT/MUSE, and Magellan AO. Current wavefront sensing and adaptive optics correction at optical wavelengths empirically depend on airmass, and Subaru/VAMPIRES provide great opportunities for Hα high-contrast imaging for Northern Hemisphere targets. © *The Authors. Published by SPIE under a Creative Commons Attribution 4.0 Unported License. Distribution or reproduction of this work in whole or in part requires full attribution of the original publication, including its DOI.* [DOI: 10.1117/1.JATIS.6.4.045004]

1 Introduction

Observing hydrogen lines provides fruitful opportunities to investigate mass accretion, shocks, jets, atmospheres, and other astrophysical phenomena. A variety of observations have been implemented, but previous observations basically targeted an isolated object or multi-objects that can be spatially resolved under seeing-limited conditions. An improvement in instrumentation has enabled better angular resolution than set by the seeing limit—adaptive optics (AO)[1] systems can make real-time corrections to wavefront distortions by the Earth's atmosphere using a guide star and delivers a point spread function (PSF) close to the diffraction-limited one. In particular, AO is very important for high-contrast imaging of exoplanets or protoplanetary disks by removing stellar halo and instrumental speckles that bury such faint signals in the stellar halo.

---

*Address all correspondence to Taichi Uyama, tuyama@ipac.caltech.edu

Table 1 VLT/MUSE archival data of YSOs.

| Target	Association	Date (UT)	Airmass	R mag[a]	H mag[b]	FWHM (mas)
PDS 70	Centaurus	June 20, 2018	1.05	11.6	8.82	~60
CIDA-9	Taurus	November 2, 2019	1.56	15.6	11.9	~80
CI Tau	Taurus	November 6, 2019	1.60	12.2	8.43	~130
GO Tau	Taurus	November 3, 2019	1.70	14.2	9.78	~150
DS Tau	Taurus	November 2, 2019	1.74	11.8	8.60	~170

[a]UCAC4 catalog.[13]
[b]2MASS.[14]

However, the AO correction at optical wavelengths was difficult in the early years of the AO instruments because the Fried parameter ($\propto \lambda^{6/5}$)[2] is so small at optical wavelengths, and hence a large number of actuators are required across the telescope aperture and fast temporal operation for wavefront sensing. Therefore, classical AO instruments were mostly applied near-infrared (NIR) wavelengths (e.g., JHKLM band), which benefit exoplanetary science because low-mass objects have less contrast with respect to their host stars in the NIR and thus high-contrast imaging at these wavelengths provides the best sensitivity.

Recently, further improvements in instrumentation have made it possible to operate AO correction at optical wavelengths [e.g., very large telescope (VLT)/multi unit spectroscopic explorer (MUSE),[3] VLT/spectro-polarimetric high-contrast exoplanet research (SPHERE),[4] Magellan AO (MagAO),[5] and Subaru/Subaru Coronagraphic Extreme Adaptive Optics (SCExAO)[6]] and have kicked off a new era of high-contrast imaging at Hα ($\lambda = 656.28$ nm). One of the most important subjects of Hα observation with AO is active mass accretion onto protoplanets (e.g., PDS 70 bc[7,8]). Recent disk observations with ALMA or NIR polarimetric observations have shown a variety of asymmetric features within 1″ that may be related to planet formation (e.g., gap, ring, or spiral[9,10]), but the number of confirmed protoplanets is still smaller than the number of predictions of potential protoplanets. Therefore, the planet formation mechanism is still controversial, and exploring for planets at such inner regions while avoiding the stellar halo with high-performance AO correction is important. The performance at optical wavelengths with current instruments highly depends on airmass. For example, the performance of MUSE/narrow-field-mode empirically decreases with airmass ≥1.6 (MUSE manual[11]). We also checked some archival MUSE data[12] and compared airmass and full width at half maximum (FWHM) in the Hα channel (see Table 1), which confirms the degradation of AO correction at high airmass. Poor AO correction leads to ineffective post-processing to remove the stellar halo and to achieve high contrast. As VLT and MagAO are located in the Southern Hemisphere, their observations of northern targets, e.g. the Taurus star-forming region, may not have sufficient sensitivity to detect Hα in the vicinity of a star.

Here, we have installed a new observing mode of The Visible Aperture Masking Polarimetric Imager for Resolved Exoplanetary Structures (VAMPIRES) at Subaru Telescope,[15] which is the only instrument capable of Hα imaging fed by AO in the Northern Hemisphere at the moment. In this paper, we present the current performance of high-contrast Hα observations with VAMPIRES. The effective bandwidth of Hα is narrower than the widths of broadband filters used in the optical-NIR astronomy,[16,17] and thus investigating such emissions or absorption's requires a specified narrowband filter or spectroscopic instrument with $R \gtrsim 1000$. VAMPIRES adopts a narrowband filter and details of the specifications are described in Sec. 2. Section 3 presents our engineering observations and the results. Finally, we summarize our work and briefly mention future prospects with AO upgrades in Sec. 4.

2 SCExAO + VAMPIRES Specifications

The VAMPIRES instrument[15] is a module of the SCExAO instrument at the Subaru telescope.[6,18,19] SCExAO, installed behind Subaru's facility adaptive optics AO188, performs
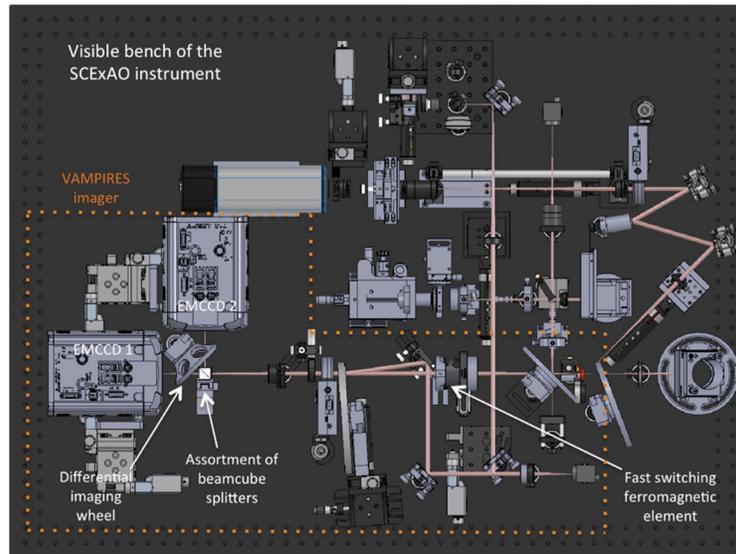
Fig. 1 Schematic view of the entire SCExAO visible bench. The VAMPIRES instrument is high-lighted by the dashed orange box.

a second stage of wavefront correction using a 2000-element deformable mirror and a visible pyramid wavefront sensor (PyWFS). The control loop typically corrects the wavefront at a frequency of 2000 Hz. The NIR light (0.95 to 2.4 μm) typically goes through a coronagraph and is recorded using the integral field spectrograph CHARIS. In median seeing conditions, SCExAO provides extreme-AO performance with NIR Strehl ratios over 80%. In visible light (600 to 900 nm), the light not used by the PyWFS is sent toward the VAMPIRES module. Optical Strehl ratio's with SCExAO depends on conditions (e.g., seeing, airmass, and brightness of a guide star) and we show examples of estimated Strehl ratios in our observations in Sec. 3.2.

VAMPIRES is capable of performing diffraction limited, polarimetric imaging at visible wavelengths (600 to 800 nm). It uses two electron-multiplying CCD (EMCCD) cameras that in normal operation each record an orthogonal polarisation, which in combination with a ferro-electric liquid crystal modulator and half-waveplate allow precise polarimetric differential imaging (PDI). The high speed of the cameras (up to ∼1000 frames/s depending on subwindow size) allows lucky imaging techniques to be used to enhance resolution, and also include non-redundant masks for super-diffraction limited imaging.

With the upgrade presented here, the polarisation-splitting optics can be automatically inter-changed for wavelength-splitting optics, recording simultaneous images in a narrowband centered at Hα ($\lambda_{cen} = 656.3$ nm, $\Delta\lambda = 1.0$ nm) in one camera and an adjacent continuum bandpass ($\lambda_{cen} = 647.68$ nm, $\Delta\lambda = 2.05$ nm) in the other. The filter information is summarized in Appendix A. The current field of view (FOV) of VAMPIRES is ∼3.3″ × 3.3″. Moreover, the choice of which of these filters is positioned in front of which camera can be rapidly switched during observation, to allow non-common path errors to be mitigated by a "double-difference" approach during data reduction (see Fig. 1 and the instrument papers for details[6,15]). The splitting of the light before encountering the filters is performed via a non-polarizing beamsplitter, to minimize mixing of polarization effects with spectral differential imaging (SDI; see Sec. 3)[20] signal.

3 Science Verification

3.1 Target Selection

For science verification, we target omicron Ceti (omi Cet) and RY Tau. These targets are reported to have Hα emissions. RY Tau is an intermediate-mass classical T Tauri Star (TTS) in the Taurus star-forming region (mass: ∼1.9$M_\odot$, age: 4.5 Myr[21]). This TTS is known to eject a jet[22,23] and

the Hα counterpart was imaged by SPHERE/zurich imaging polarimeter (ZIMPOL).[21] A omi Cet is a Mira variable star, undergoing massive stellar pulsations wherein shocks are expected to produce Hα emission.[24] While detectable in spectroscopy, this is very difficult to resolve spatially due to the expected low spatial separation (several 10 s of milliarcseconds) between the star and shock region.

We also use SAO 105500 (γ Sge) data for a comparison of the post-processing results with those of omi Cet and RY Tau. Previous spectroscopic observation proves that this single star does not present any Hα emission/absorption features[25,26] and is good for the comparison of the results.

3.2 Observation

SCExAO is operated under angular differential imaging (ADI) mode[27] by fixing the pupil, with which we can utilize a combination of SDI and the ADI technique to detect faint objects around the target star. VAMPIRES uses a beam-switcher where both filters can be converted frequently, and hence, the spectral content of the beams is switched between the two detectors. To reduce further bias, which arises from non-common path aberrations and systematic differences between the detectors, and to achieve better sensitivity, we utilize double differential imaging (DDI)[28] techniques for SDI reduction (see also Figs. 2 and 3 for the schematic of the post-processing). To calibrate the plate scale, we imaged astrometric binaries HD 117902 and HIP 17954 and measured plate scale to be 6.475 ± 0.09 mas/pix.

We observed SAO 105500, omi Cet, and RY Tau in our engineering runs on May 22, 2019, September 8, 2019, and January 31, 2020 UT, respectively. Table 2 summarizes our observations used in this study and Table 3 summarizes the Strehl ratios of our data. We used the beginning part of these data sets for measuring them. To estimate the Strehl ratio we (1) computed the ratio between the total flux inside the core of the PSF ($2.44\lambda/D$ in diameter) and the total flux of the PSF inside a circle of $85\lambda/D$ (to reject the diffraction pattern created by the quilting mode of the deformable mirror) and (2) computed the same ratio calculated for a simulated perfect PSF using the shape and orientation of the pupil. Then, the Strehl ratio is the flux ratio of the on-sky image divided by the flux ratio of the simulated image. The Strehl ratios measured from the single exposures indicate the performance of the "fast-AO correction" with SCExAO + VAMPIRES. For comparison, we also show the Strehl ratios with the long exposure (simply cube-combined PSF without image registration). We note that at the data reduction stage, we do image registration of each slice and then conduct the post-processing technique (see
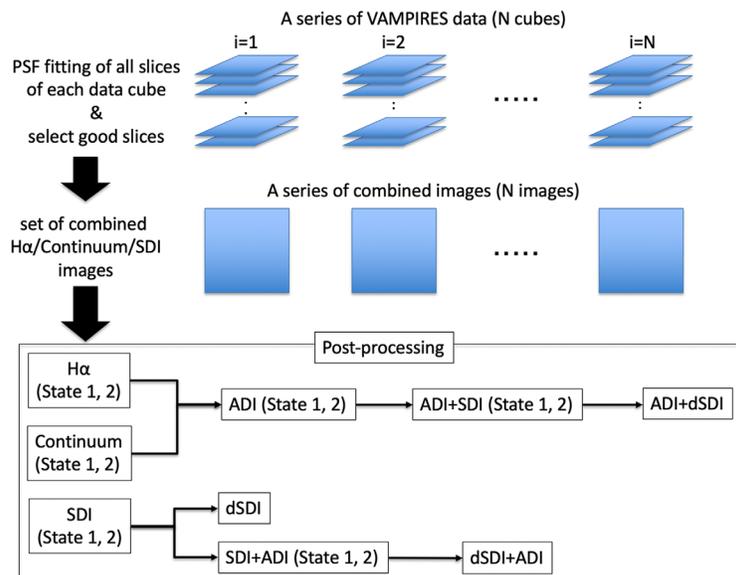
Fig. 2 Flowchart of data reduction from VAMPIRES data cube through final outputs. Keyword "dSDI" corresponds to double-SDI.
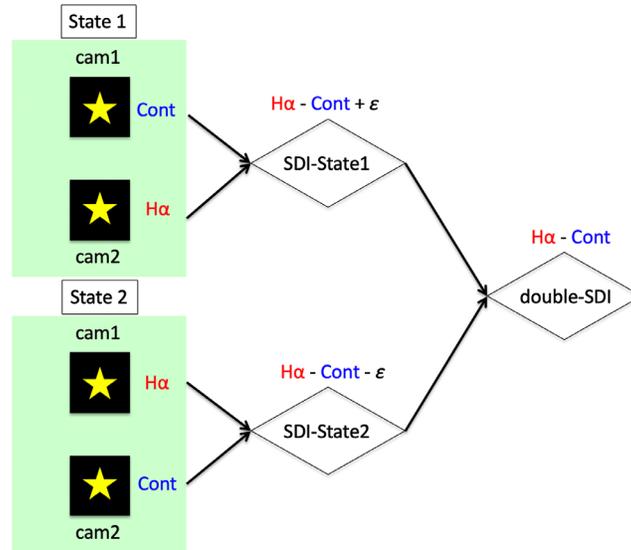
Fig. 3 Schematic of dSDI with VAMPIRES Hα mode. "Hα," "Cont," and "ε" correspond to Hα, continuum flux, and bias between cam2 and cam1, respectively. In the state 1, we subtract the cam1 (continuum) image from the cam2 (Hα) image, and in the state 2, we do the other way around.

Table 2 Observing logs.

| | | | | | t_{total} (s) | | |
| | | Seeing | | R | | | |
Target	Date (UT)	(″)[a]	Airmass	mag	State 1	State2	Remarks
SAO 105500	May 22, 2019	0.62	1.07	2.23[b]	256.16[c]	256.16[c]	No ADI
omi Cet	September 8, 2019	0.70	1.15	4.34[d]	463.96[e]	448.14[f]	Smaller FOV[g]
RY Tau	January 31, 2020	0.66	1.01	9.05[d]	2497[h]		State 1 only, no DDI

[a]Mean DIMM seeing at the summit of Mauna Kea.
[b]Johnson R-band photometry.[29]
[c]20 ms/slice × 1601 slices/cube × 8 cubes.
[d]These targets are variable at optical wavelength and we adopt photometric data provided by Ref. 30 on the nearest date to our observations.
[e]20 ms/slice × 3201 slices/cube × 7 cubes + 20 ms/slice × 791 slices/cube × 1 cube.
[f]20 ms/slice × 3201 slices/cube × 7 cubes.
[g]~1.65″ × 1.65″.
[h]1 s/slice × 101 slices/cube × 24 cubes + 1 s/slice × 73 slices/cube × 1 cube.

Sec. 3.3), the performance of which is indicated in the last column of Table 3. For the SAO 105500 and RY Tau data, we see the same characteristics in that the top 5% PSF has the highest Strehl ratio. The single exposure of RY Tau has lower signal-to-noise ratio (SNR) because this target is faint in the optical wavelength, which may affect the background evaluation and the Strehl ratio measurement. For the omi Cet data, the long-exposure PSF has the highest Strehl ratio, but this is likely related to measurement errors of the Strehl ratio and the background: we combined 3201 slices to make the long-exposure image (and ~2880 slices to make the combined image) and the background values are much better estimated than the single-exposure images.

Figure 3 shows difference between state 1 (cam1: continuum, cam2: Hα) and state 2 (cam1: Hα, cam2: continuum) so that we can conduct the DDI technique to reduce the effects of the non-common path aberrations, which is explained in Sec. 3.3.1. The VAMPIRES output constitutes a data cube (x, y, and time) and exposure time/cube format information is summarized in Table 2. It is worth noting that we replaced an Hα narrowband filter before the RY Tau observation and we observed SAO 105500 and omi Cet with a different Hα filter ($\lambda = 656.4$ nm, $\Delta\lambda = 2.0$ nm).

Table 3 Strehl ratios.

| Target | Short exposure[a] | | | | Long exposure[b] | | Shift and combined[c] |
	t_{eq} (s)[d]	5% percentile	30% percentile	50% percentile	t_{eq} (s)[d]		
SAO 105500	0.02	~44%	~40%	~35%	32.02	~35%	~39%
omi Cet	0.02	~41%	~39%	~37%	64.02	~45%	~44%
RY Tau	1	~9%	~8%	~6%	101	~8%	~9%

[a]We selected the single exposures whose PSFs have 5%, 30%, and 50% percentile peaks among all the single exposures using the fitted PSF information and then estimated the Strehls from these selected PSFs. This value indicates the performance of the short-exposure AO correction.
[b]We combined a data cube into an image without image registration. This value indicates the performance of the long-exposure AO correction (exposure time corresponds to the product of the single exposure time and the number of slices in the data cube, see also Table 2).
[c]We selected a set of slices in a data cube (top 90% peaks), and then shifted all the images to align the center of the PSF, and finally combined them to make the combined image. This data set is basically used for the post-processing in this study.
[d]Equivalent integration time.

3.3 Data Reduction

As SCExAO + VAMPIRES enables fast-AO correction, we can obtain images with very short exposures. Then we can select "good" PSFs among all the data set like lucky imaging. After dark subtraction, we read all continuum slices, which do not basically include any asymmetric features related to Hα from the central star, to fit PSFs for good-data selection and image registration. We used a criterion of fitted peak and selected 90% good data sets that would then be reduced by post-processing. The typical FWHMs of the selected data sets were 45 mas (7 pix) and 55 mas (8.5 pix) for omi Cet and RY Tau, respectively. Hereafter, we show several methods of reducing the data by combining the ADI and SDI techniques to look for differences in the outputs because, for instance, a previous VLT/spectrograph for integral field observations in the near infrared observation[31] suggested a specific order to utilize ADI and SDI reduction techniques may change the overall sensitivity.

3.3.1 SDI and SDI + ADI

The advantage of the SDI reduction is that in principle we can subtract continuum components as a reference PSF from the Hα image that includes both Hα and continuum information. AO correction works with almost the same efficiency in both filter bands and enables us to simply subtract the continuum image from the Hα image after correcting throughputs between cameras and filter transmission functions. The coefficients used for the throughput correction are assessed by comparing photometric results of instrumental laser PSFs.

Figure 2 shows a flowchart of data reduction, and Fig. 3 shows a brief schematic of the double-SDI (dSDI) reduction with VAMPIRES, respectively. VAMPIRES data consist of two states where the Hα and continuum filters are switched with each other. Subtracting an image taken at one of the detectors from the other image leaves non-common path aberrations, which corresponds to the bias (ϵ) in Fig. 3. Applying the DDI technique to the SDI reduction can further suppress the effects of the bias on the final-reduced image. After PSF fitting of continuum slices using the Moffat function,[32] we repeat producing an SDI-reduced slice by subtracting a good-continuum slice in the VAMPIRES data cube from a corresponding Hα slice, which can attenuate the influence of the atmospheric turbulence at each short exposure. Here, we used the fitted peak of each PSF as a criterion for judging good PSFs.

SDI reduction. Next, we made a combined SDI-reduced image per data cube. As SCExAO is operated in ADI mode, we derotate images by differences of parallactic angle and then combine this data set into an SDI-reduced image. At each state, we conduct SDI reduction and finally obtain dSDI-reduced image using two SDI-reduced images. We note that in this study we

mainly intend to reduce the continuum component from the Hα image and that we do not scale the reference (continuum) image by the difference of wavelength from Hα to attenuate the speckle noise.

SDI + ADI reduction. By applying the ADI technique to the residual of the SDI result, we can further suppress the speckle noise. The data set of combined SDI-reduced image per data cube can also be applied to ADI reduction (see Sec. 3.3.2), which leads to two SDI + ADI images in state 1 and 2. We then conduct double-differential imaging to obtain the final dSDI + ADI image.

3.3.2 *ADI + SDI*

ADI makes a likely reference PSF that includes the starlight and instrumental speckles by rotating the FOV, then subtracting it from the raw images, and finally derotating and combining the subtracted images. This post-processing technique has been widely used for high contrast imaging and has been used to detect faint companions and/or other asymmetric features within a few arc sec. We made a set of images by combining selected good slices among one data cube, which is then input into ADI reduction algorithms. In this paper, we utilized Karhunen-Loéve Image Projection algorithms (KLIP)[33] with pyKLIP algorithms[34] to produce the most likely reference PSF from the set of combined SDI-reduced images, where we adopted optimization and subtraction area as large as the whole VAMPIRES FoV.

After PSF fitting of continuum slices, we made both combined continuum and Hα images per data cube. Then, we applied pyKLIP to four data sets (registered images of continuum/Hα in state 1/2). Each reduced image was then used for further dSDI reduction (see Fig. 3) and we finally got the ADI + dSDI image. We note that the ADI + SDI reduction substantially ignores the advantage of simultaneous acquisition of Hα and continuum at each exposure.

3.4 *Results*

We present a variety of results that were reduced via SDI and ADI reduction techniques. We note that in this study, we do not analyze Hα intensities of each detection and discuss mechanisms of (possible) Hα emissions from omi Cet, omi Cet B, and RY Tau.

3.4.1 *Omi Cet*

Figure 4(a) shows a single exposure raw Hα image of omi Cet. We note that omi Cet B was detected in both combined Hα and continuum images from one data cube [see Figs. 4(b) and 4(c)]. Figures 4(d) and 4(e) compare the SDI-reduced images of state 1 and 2, respectively. Figure 4(f) shows the dSDI result, and Fig. 5 plots an azimuthally-averaged radial profile of the dSDI result. There is a ring-like feature at a separation of ∼0.03″. We also checked encircled energy of both combined Hα and continuum images, and Hα profile is slightly brighter than the continuum profile at ∼0.03″ (see Fig. 6), though the difference is marginal compared with the Hα and continuum observations of η Carinae.[35] This feature represents either of the expected astrophysical feature—limb brightening of the shock feature at Hα—or the difference of PSFs at wavelengths between the Hα and the continuum filters. To further test whether our data reduction can be affected by an artifact (e.g. different AO correction), we apply the dSDI reduction to the SAO 105500 data (see Sec. 3.4.3 for the result). A scientific analysis of these resolved observations of the Hα shock region will be presented in a forthcoming paper.

Figure 7 compares the outputs of combining ADI and dSDI reduction techniques. For ADI reduction, we adopted KL = 3 to show our outputs because we had a small number of data cubes and the larger KL number does not work properly. The smaller number of KL modes subtracts the starlight less efficiently and thus leaves a lot of residuals. Both of the reduction approaches resulted in almost the same outputs and detected omi Cet B with SNRs >5000, but with the ADI + dSDI reduction [Fig. 7(b)], there still remains some stellar halo at the inner working angle. The noise was estimated by calculating the standard deviation within an annular region at different separations, which is used for signal-to-noise (SN) maps and detection limits.
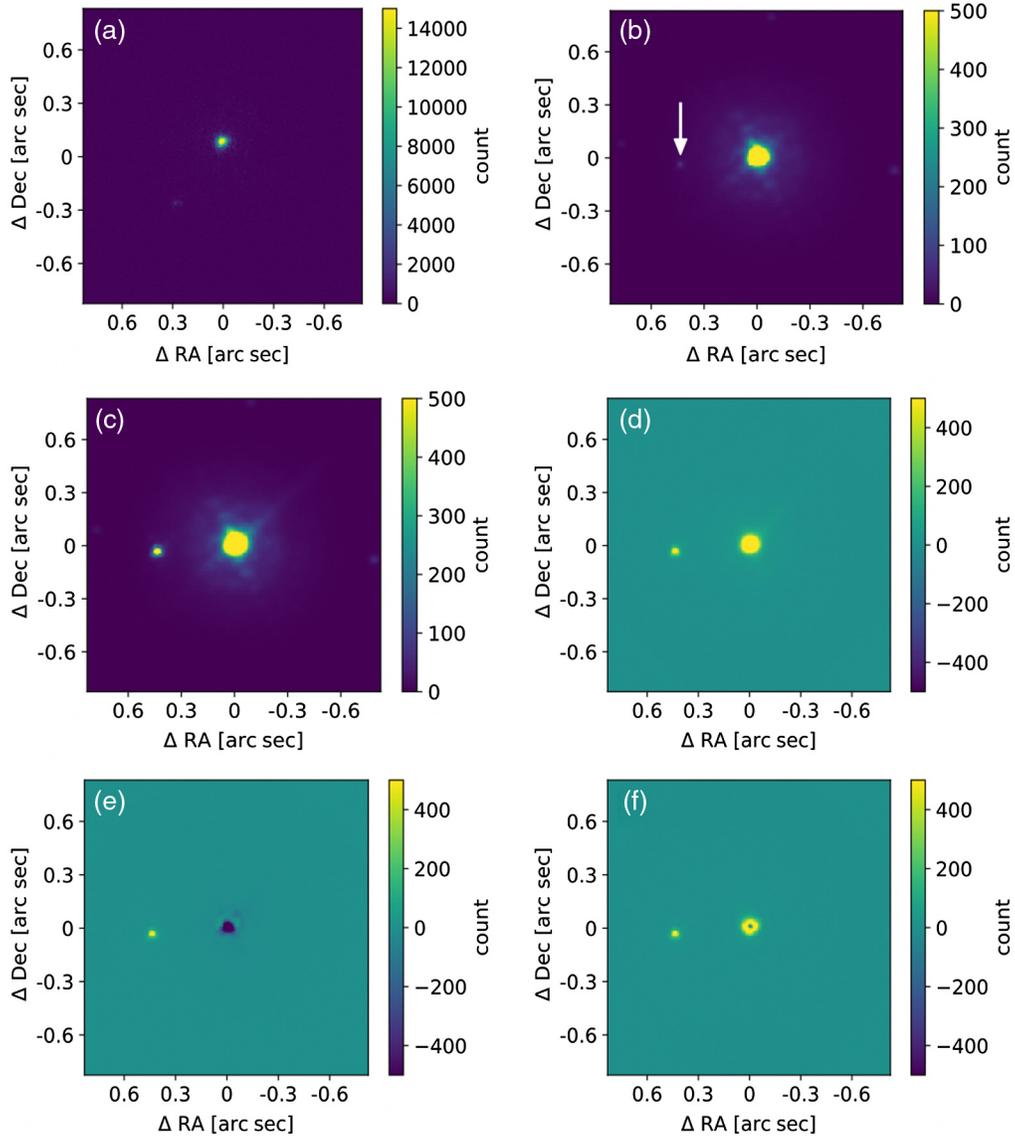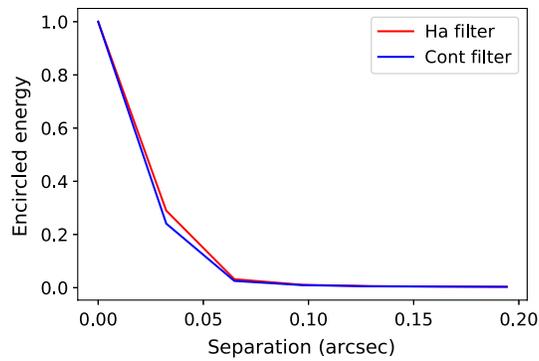
Fig. 4 Flowchart of the SDI reduction for the omi Cet data. (a) Single Hα image of omi Cet (exposure time = 20 ms) before the dark subtraction. (b) Combined continuum image of omi Cet from a single data cube at state 1. The location of omi Cet B is indicated by a white arrow. (c) Combined Hα image of omi Cet from a single data cube at state 1. The companion (omi Cet B) is located east. (d) SDI-reduced image (Hα-continuum) of state 1. (e) SDI-reduced image (Hα-continuum) of state 2. The bias made the apparent result different from the SDI result of state 1 (d). (f) dSDI result of omi Cet. A ring feature is visible around the central star, corresponding to the expected shock arising from the stellar pulsations.

Figure 8 compares 5σ detection limits as a function of separation. The right vertical axis corresponds to apparent flux converted from contrast (erg/s/cm^2) assuming the R-band flux for omi Cet. The humps at 0.4″ to 0.5″ seen in the limits of dSDI + ADI and ADI + dSDI are affected by the existence of omi Cet B. Regarding the throughput calculation to correct flux loss by the post-processing, we assumed that a companion can be detected in only Hα wavelength and that SDI reduction does not lose the signal of Hα. Therefore, we injected fake sources in the Hα images and calculated the throughputs of ADI reduction. In case, a companion is detected in both continuum and Hα filters, such as omi Cet B, it is better to use photometric results from both combined Hα and continuum images to accurately obtain Hα intensity.
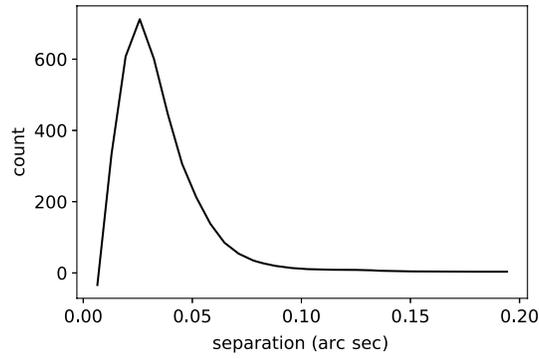
Fig. 5 Azimuthally-averaged radial profile of surface brightness around omi Cet after the dSDI reduction [see Fig. 4(f)].


Fig. 6 Comparison of the encircled energies for combined Hα [red, Fig. 4(c)] and continuum [blue, Fig. 4(b)] images. The Hα profile is brighter than that of the continuum profile at ∼0.03″.
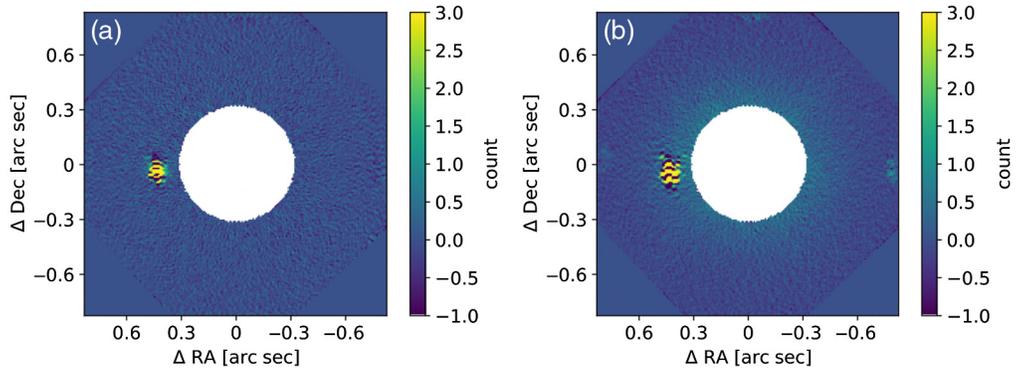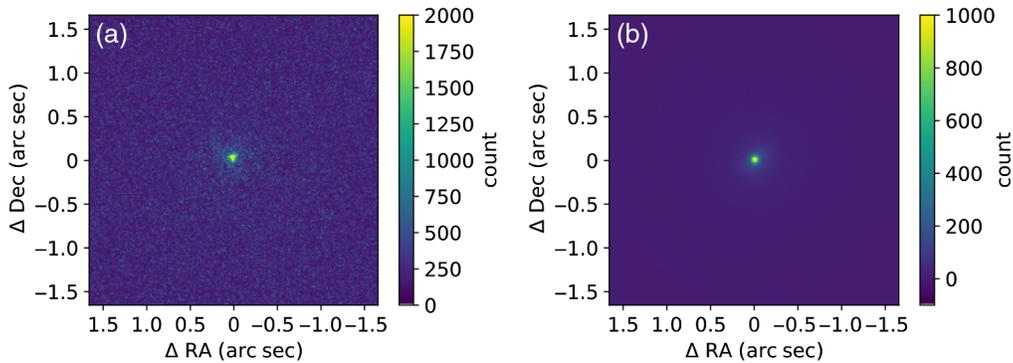

Fig. 7 Flowchart of combining ADI and dSDI for the omi Cet data. (a) ADI-reduced image (KL = 3) after implementing dSDI reduction (dSDI + ADI). Central star is masked by the algorithm. (b) dSDI-reduced image after implementing ADI (KL = 3) reduction (ADI + dSDI).

3.4.2 *RY Tau*

Figure 9(a) shows a single exposure raw Hα image of RY Tau. Figures 9(b) and 10(a) show SDI-reduced and ADI-reduced images of state 1. We note that RY Tau observation took only state 1, and we did not conduct the DDI reduction. Figures 10(c) and 10(e) compare the outputs of
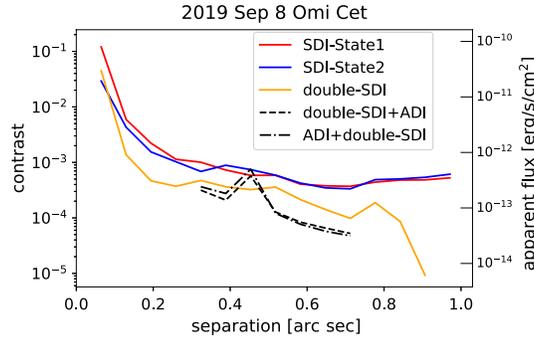
Fig. 8 Comparison of 5σ contrast limits of omi Cet data with a variety of reduction methods. "dSDI + ADI" and "ADI + dSDI" correspond to running ADI reduction after dSDI reduction [Fig. 7(a)] and the reverse order [Fig. 7(b)], respectively.
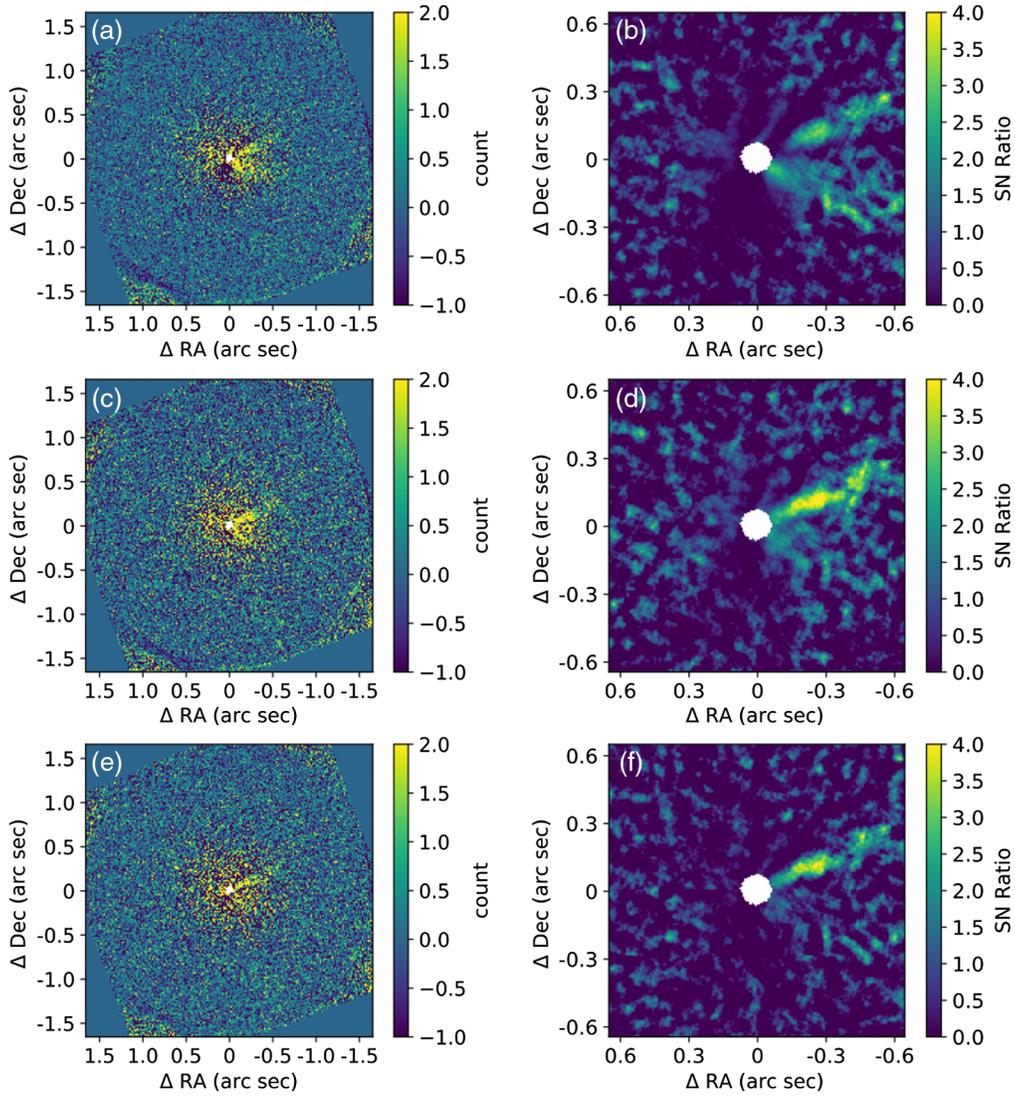

Fig. 9 Flowchart of the SDI reduction for the RY Tau data. (a) Single Hα image of RY Tau (exposure time = 1 s) before the dark subtraction. (b) SDI-reduced image of RY Tau.

combining ADI and dSDI reduction techniques. For ADI reduction we adopted KL = 5 to show our outputs. Both of the reduction ways detected the jet with SNR ∼ 4 to 5, but its SNR is slightly higher in the SDI + ADI result [Fig. 10(c)]. Figures 10(b), 10(d), and 10(f) show cropped SN maps of Figs. 10(a), 10(c), and 10(e), respectively. Indeed a simple ADI reduction could detect the same feature to some extent as seen in the SDI + ADI image, but there is another feature that corresponds to speckles because of insufficient AO correction at optical wavelengths.

The most significant feature in our post-processed image extends ∼0.3″, which is consistent with the SPHERE/ZIMPOL Hα observation.[21] The SPHERE observation also reported a fainter and more extended Hα region extending ∼1″, and our SDI + ADI-reduced image marginally confirms the inner part ($\rho \sim 0.3″ − 0.6″$) of this feature with SNR ∼ 3.

Figure 11 compares 5σ detection limits as a function of separation. At larger separations ($\rho \gtrsim 0.5″$) ADI reduction achieved higher contrast than the combination of ADI and SDI reduction because subtracting continuum image (camera 1) from Hα image (camera 2) leaves the bias that increases the background noise. At inner separations ($\rho \lesssim 0.3$), the detection limit of SDI + ADI looks worse than that of ADI + SDI, but this feature may be affected by higher SNR of the jet. From a point of view of contrast, the omi Cet observation (Fig. 8) achieved higher contrast than the RY Tau observation because of better wavefront sensing and AO correction, but RY Tau observation could achieve deeper detection limits in apparent flux. For future observations, the beam switching with VAMPIRES and DDI reduction will help to achieve a better contrast level than the RY Tau result. Compared with other Hα high-contrast imaging observations, SCExAO + VAMPIRES has a similar sensitivity of Hα to SPHERE/ZIMPOL,[36,37] MagAO,[7] and MUSE[8] and provides great opportunities for high-contrast Hα imaging in the Northern Hemisphere.

Fig. 10 Flowchart of combining ADI and SDI for the RY Tau data. (a) ADI-reduced Hα image. (b) Cropped SN map of (a). (c) ADI-reduced image after implementing SDI reduction. (d) Cropped SN map of (c). (e) SDI-reduced image after implementing ADI reduction. (f) Cropped SN map of (e).
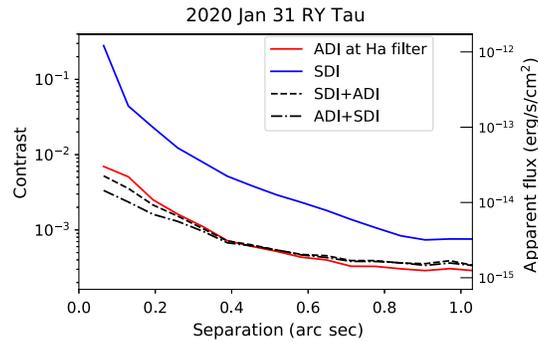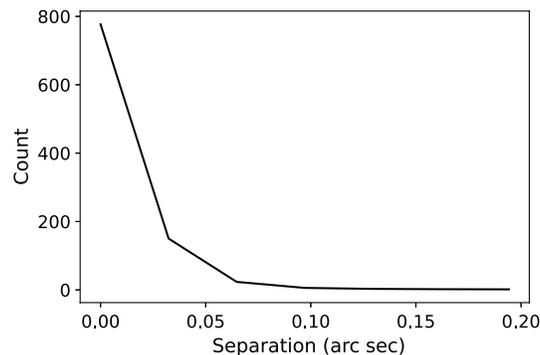

Fig. 11 Comparison of 5σ contrast limits of RY Tau data with a variety of reduction methods. "SDI + ADI" and "ADI + SDI" correspond to running ADI reduction after SDI reduction [Fig. 10(c)] and the reverse order [Fig. 10(e)], respectively.
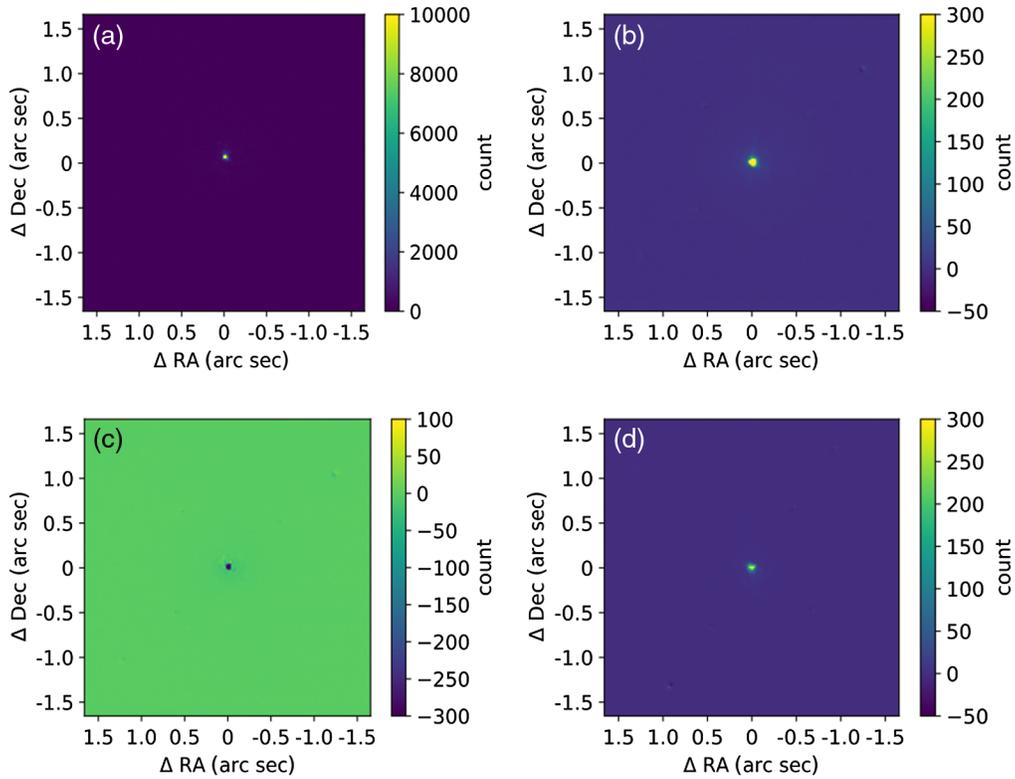
Fig. 12 Flowchart of the SDI reduction for the SAO 105500 data. (a) Single Hα image of SAO 105500 (exposure time = 20 ms) before the dark subtraction. (b) SDI-reduced image of state1. (c) SDI-reduced image of state2. The bias made the apparent result different from the SDI result of State 1 (b). (d) dSDI-reduced image of SAO 105500.
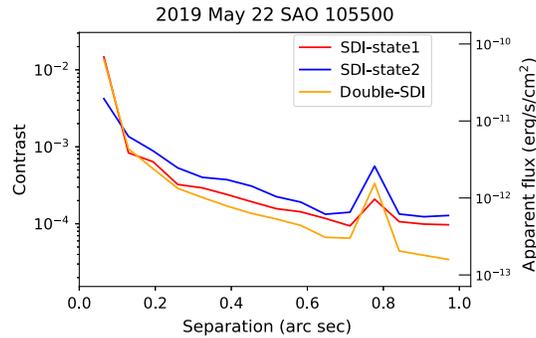
3.4.3 *SAO 105500*

For comparing the post-processing results of the other two targets, we reduced the SAO 105500 data. We note that because of small field rotation, we could not conduct the ADI reduction and we show the SDI results in this section. Figures 12(a)–12(d) show the single Hα image and the SDI-state1, SDI-state2, and dSDI results, respectively. We see the same tendency of the positive/ negative counts at the central star at the SDI-reduced images in state 1/2 as the case of omi Cet [Figs. 4(d) and 4(e)]. The residual at the center probably reflects the difference of its spectrum at wavelengths of the Hα-filter and the continuum-filter. Figure 13 shows an azimuthally-averaged radial profile of the surface brightness, and there is no ring-like feature as seen in the case of

Fig. 13 Azimuthally-averaged radial profile of surface brightness around SAO 105500 after the dSDI reduction [see Fig. 12(d)].
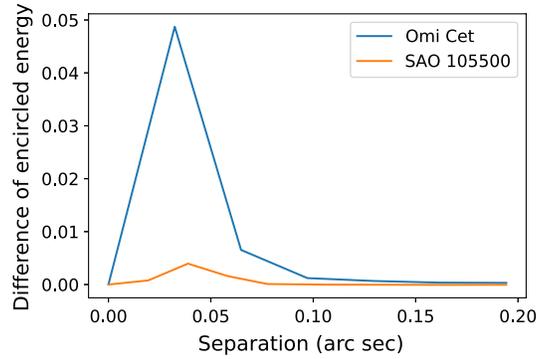
Fig. 14 Difference of the encircled energies between Hα and continuum PSFs.

Fig. 15 Comparison of 5σ contrast limits of SAO 105500 data with a variety of reduction methods.

omi Cet [Fig. 4(f)]. Figure 14 compares difference of the encircled energies between Hα and continuum PSFs. The slight rise in the SAO 105500 profile by ∼0.4% at 0.3″ is likely caused by the difference of AO correction at Hα and continuum wavelengths. The omi Cet profile has much greater difference by ∼5% at 0.3″. Considering that AO correction to SAO 105500 works as effectively as to omi Cet, the difference profile at omi Cet may not only be affected by the difference of AO correction. We need to model the expected Hα shock around omi Cet to discuss in detail as mentioned in Sec. 3.4.1.

We also show the 5σ detection limits of the SAO 105500 data in Fig. 15. The humps at ∼0.8″ are affected by diffraction patterns arising from the bright central star. These detection limits reach similar contrast levels to the omi Cet case because of almost the same AO efficiency.

4 Summary and Future Prospects

We present high-contrast Hα observations with Subaru/SCExAO + VAMPIRES. VAMPIRES adopts the beam-switching system where we can efficiently conduct SDI reduction by utilizing DDI technique. We also show the combination of ADI reduction with SDI with our engineering data sets of omi Cet and RY Tau. Our dSDI reduction could resolve a ring feature around omi Cet (corresponding to the expected shock arising from this star's pulsations) and detect omi Cet B in both continuum and Hα filter, and SDI + ADI reduction could resolve a jet around RY Tau. We achieved ∼10^{-4} at 0.5″ for omi Cet and ∼5×10^{-4} at 0.5″ for RY Tau, respectively. Our detection limits in apparent flux are comparable to other high-contrast Hα imaging with SPHERE/ZIMPOL, MUSE, and MagAO located in the Southern Hemisphere. Our instrument will provide great opportunities of implementing high-contrast Hα explorations of northern targets.

In the next few years, AO188 will benefit from two major upgrades that will benefit SCExAO and VAMPIRES. AO188's 188-element deformable mirror will be replaced with a 64 × 64-

element deformable mirror, which will improve significantly the wavefront correction at all wavelengths. The second upgrade is the addition of an NIR PyWFS inside AO188, which will be used to probe redder targets such as TTS.[38] SCExAO is also being upgraded to perform PDI at NIR wavelengths, using a fast detector similarly to VAMPIRES, and also by doing spectro-polarimetry using CHARIS. A differential imaging mode is also envisioned to include an SDI mode at the Paβ (1.28 μm) wavelength. In case of planet formation, for instance, theoretical models suggest that hydrogen emissions depend on several parameters such as number density of hydrogen, pre-shock velocity, extinction of the source, and filling factor of the emission[39] and obtaining only Hα cannot solve degeneracy between these parameters. Therefore Paβ will help to solve the degeneracies and promote detailed discussions of accretion mechanisms. Currently, a limited number of instruments enable high-contrast imaging explorations of Paβ (e.g., Keck/OH-suppressing infra-red imaging spectrograph[40]) and SCExAO will be more useful instruments for hydrogen emission observations.

5 Appendix A: Filter Information

Figure 16 summarizes the narrow-band filters we used in this study. The Hα filter was replaced in January 2020. For high-contrast Hα imaging with VAMPIRES, we designed the bandpass of the filter to be able to transmit sufficient signal in light of various broadening effects. For example, the maximum accretion velocity of a Jupiter mass planet is ∼60 km/s. To account for an object larger than a Jovian planet, we adopted a velocity of ±100 km/s. In addition, the radial velocity (RV) motion of a planet around such a star is ≲10 km/s, and the RV motion of the star from the observer is ≲50 km/s. Therefore, we set a budget of 200 km/s, which corresponds to a 0.8-nm wavelength range at 600 nm, which should cover all the astrophysical features one may like to study.

We found an off-the-shelf filter from Chroma that had specifications very close to our requirements (3-nm bandwidth; see also the manuscript webpage at Chroma[41]) and requested it be modified to have an FWHM bandwidth of 2 nm instead. This is still larger than the 0.8 nm needed and was chosen because of the uncertainty the manufacturer offered in the center wavelength of the filter and our ability to align it with respect to the beam. This filter was purchased and installed. However, the VLT/MUSE observation to study accretion from PDS 70 bc revealed that the effective width of Hα is ∼100 to 120 km/s.[8,42] We found that detecting such a signal with the 2-nm bandwidth filter will require higher contrast, enough to detect the accreting planet. Therefore, we decided to replace the previous Hα filter with a new filter (1-nm bandwidth) in January 2020. This bandwidth is the minimum acceptable value for the Hα imaging with our assumptions. Out of band, the optical density (OD) of the new Hα filter is larger than 4 (OD4 means that the out-of-band suppression is 0.01%) across 400 to 1200 nm, which covers the entire bandpass of the EMCCD. Similarly, the suppression of the old Hα and continuum filters was better than OD5 (the out-of-band suppression is 0.001%) from 400 to 1000 nm. The detailed information for the new Hα filter is shown at Alluxa.[43]
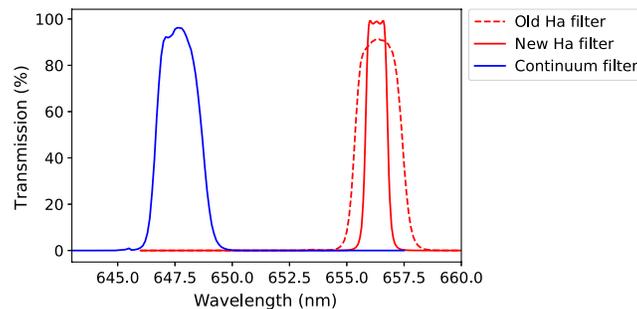
Fig. 16 Transmission curves of the narrowband filters used in this study. The old Hα filter was used for the SAO 105500 and omi Cet observation, and the new Hα filter was used for the RY Tau observation. The continuum filter has not been replaced.

Acknowledgments

References

1. J. M. Beckers, "Adaptive optics for astronomy: principles, performance, and applications," *Ann. Rev. Astron. Astrophys.* **31**, 13–62 (1993).
2. D. L. Fried, "Statistics of a geometric representation of wavefront distortion," *J. Opt. Soc. Am. (1917-1983)* **55**, 1427–1431 (1965).
3. R. Bacon et al., "The MUSE second-generation VLT instrument," *Proc. SPIE* **7735**, 773508 (2010).
4. J. L. Beuzit et al., "SPHERE: the exoplanet imager for the Very Large Telescope," *Astron. Astrophys.* **631**, A155 (2019).
5. J. R. Males et al., "Magellan adaptive optics first-light observations of the exoplanet Pic B. I. Direct imaging in the far-red optical with MagAO + VisAO and in the near-IR with NICI," *Astrophys. J.* **786**, 32 (2014).
6. J. Lozi et al., "SCExAO, an instrument with a dual purpose: perform cutting-edge science and develop new technologies," *Proc. SPIE* **10703**, 1070359 (2018).
7. K. Wagner et al., "Magellan adaptive optics imaging of PDS 70: measuring the mass accretion rate of a young giant planet within a gapped disk," *Astrophys. J.* **863**, L8 (2018).
8. S. Y. Haffert et al., "Two accreting protoplanets around the young star PDS 70," *Nat. Astron.* **3**, 749–754 (2019).
9. S. M. Andrews et al., "The Disk Substructures at High Angular Resolution Project (DSHARP). I. Motivation, sample, calibration, and overview," *Astrophys. J.* **869**, L41 (2018).
10. R. Dong, J. R. Najita, and S. Brittain, "Spiral arms in disks: planets or gravitational instability?" *Astrophys. J.* **862**, 103 (2018).
11. European Southern Observatory (ESO), "MUSE documentation," https://www.eso.org/sci/facilities/paranal/instruments/muse/doc.html.
12. ESO, "ESO science archive facility," http://archive.eso.org.
13. N. Zacharias et al., "VizieR online data catalog: UCAC4 catalogue (Zacharias+, 2012)," VizieR Online Data Catalog, I/322A (2012).
14. R. M. Cutri et al., "VizieR online data catalog: 2MASS all-sky catalog of point sources (Cutri+ 2003)," VizieR Online Data Catalog, II/246 (2003).
15. B. Norris et al., "The VAMPIRES instrument: imaging the innermost regions of proto-planetary discs with polarimetric interferometry," *Mon. Not. R. Astron. Soc.* **447**, 2894–2906 (2015).
16. A. T. Tokunaga, D. A. Simons, and W. D. Vacca, "The Mauna Kea observatories near-infrared filter set. II. Specifications for a new 'JHKLM' filter set for infrared astronomy," *Publ. Astron. Soc. Pac.* **114**, 180–186 (2002).
17. M. Doi et al., "Photometric response functions of the sloan digital sky survey imager," *Astrophys. J.* **139**, 1628–1648 (2010).

18. N. Jovanovic et al., "The Subaru Coronagraphic Extreme Adaptive Optics system: enabling high-contrast imaging on solar-system scales," *Publ. Astron. Soc. Pac.* **127**, 890 (2015).

19. T. Currie et al., "Performance and early science with the Subaru Coronagraphic Extreme Adaptive Optics project," *Proc. SPIE* **11117**, 111170X (2019).

20. W. H. Smith, "Spectral differential imaging detection of planets about nearby stars," *Publ. Astron. Soc. Pac.* **99**, 1344–1353 (1987).

21. A. Garufi et al., "SPHERE view of the jet and the envelope of RY Tauri," *Astron. Astrophys.* **628**, A68 (2019).

22. S. Cabrit et al., "Forbidden-line emission and infrared excesses in T Tauri Stars: evidence for accretion-driven mass loss?" *Astrophys. J.* **354**, 687 (1990).

23. V. Agra-Amboage et al., "[O I] sub-arcsecond study of a microjet from an intermediate mass young star: RY Tauri," *Astron. Astrophys.* **493**, 1029–1041 (2009).

24. D. Gillet, E. Maurice, and D. Baade, "The shock-induced variability of the H alpha emission profile in Mira," *Astron. Astrophys.* **128**, 384–390 (1983).

25. G. A. Alekseeva et al., "The Pulkovo spectrophotometric catalog of bright stars in the range from 320 to 1080 nm. a supplement," *Baltic Astron.* **6**, 481–496 (1997).

26. M. Wittkowski et al., "Tests of stellar model atmospheres by optical interferometry. III. NPOI and VINCI interferometry of the M0 giant Sagittae covering 0.5–2.2 m," *Astron. Astrophys.* **460**, 843–853 (2006).

27. C. Marois et al., "Angular differential imaging: a powerful high-contrast imaging technique," *Astrophys. J.* **641**, 556–564 (2006).

28. S. Hinkley et al., "Speckle suppression through dual imaging polarimetry, and a ground-based image of the HR 4796A circumstellar disk," *Astrophys. J.* **701**, 804–810 (2009).

29. Y. Huang et al., "Empirical metallicity-dependent calibrations of effective temperature against colours for dwarfs and giants based on interferometric data," *Mon. Not. R. Astron. Soc.* **454**, 2863–2889 (2015).

30. American association of variable star observers (AAVSO), "AAVSO," https://www.aavso.org/.

31. V. Christiaens et al., "Separating extended disc features from the protoplanet in PDS 70 using VLT/SINFONI," *Mon. Not. R. Astron. Soc.* **486**, 5819–5837 (2019).

32. A. F. J. Moffat, "A theoretical investigation of focal stellar images in the photographic emulsion and application to photographic photometry," *Astron. Astrophys.* **3**, 455 (1969).

33. R. Soummer, L. Pueyo, and J. Larkin, "Detection and characterization of exoplanets and disks using projections on Karhunen—Loève Eigenimages," *Astrophys. J.* **755**, L28 (2012).

34. J. J. Wang et al., "pyKLIP: PSF subtraction for exoplanets and disks," https://ui.adsabs.harvard.edu/abs/2015ascl.soft06001W/abstract (2015).

35. Y.-L. Wu et al., "Resolving the H-emitting region in the wind of η Carinae," *Astrophys. J.* **841**, L7 (2017).

36. G. Cugno et al., "A search for accreting young companions embedded in circumstellar disks. High-contrast H imaging with VLT/SPHERE," *Astron. Astrophys.* **622**, A156 (2019).

37. A. Zurlo et al., "The widest H survey of accreting protoplanets around nearby transition disks," *Astron. Astrophys.* **633**, A119 (2020).

38. C. Z. Bond et al., "Adaptive optics with an infrared pyramid wavefront sensor," *Proc. SPIE* **10703**, 107031Z (2018).

39. Y. Aoyama and M. Ikoma, "Constraining planetary gas accretion rate from H line width and intensity: case of PDS 70 b and c," *Astrophys. J.* **885**, L29 (2019).

40. T. Uyama et al., "Constraining accretion signatures of exoplanets in the TW Hya transitional disk," *Astron. J.* **154**, 90 (2017).

41. CHROMA, "27001 - H-alpha 3nm bandpass," https://www.chroma.com/products/parts/h-alpha-3nm-bandpass.

42. J. Hashimoto et al., "Accretion properties of PDS 70b with MUSE," *Astron. J.* **159**, 222 (2020).

43. Alluxa, "656.3-1 OD4 ultra narrow bandpass filter," https://www.alluxa.com/optical-filter-catalog/ultra-narrow-bandpass/656-3-1-od4-ultra-narrow-bandpass.html.

Taichi Uyama studied astronomy at the University of Tokyo, Japan, and received his PhD in 2019. Now he works at Caltech/IPAC as a postdoc in a field of high-contrast imaging of exoplanets/proplanetary disks.

Biographies of the other authors are not available.